Chemical Engineering Journal 292 (2016) 123–129

Contents lists available at ScienceDirect

Chemical Engineering Journal

journal homepage: www.elsevier.com/locate/cej

Enhancement of heterogeneous oxidation and adsorption of Hg^0 in a wide temperature window using SnO_2 supported $LaMnO_3$ perovskite oxide

Haomiao Xu, Zan Qu, Songjian Zhao, Dongting Yue, Wenjun Huang, Naiqiang Yan *

School of Environmental Science and Engineering, Shanghai Jiao Tong University, Shanghai 200240, China

HIGHLIGHTS

- SnO_2 was used as catalyst support for $LaMnO_3$.
- The reaction temperature window was enlarged over $LaMnO_3/SnO_2$.
- The Hg^0 removal efficiencies were enhanced by adding SnO_2 support.
- The mechanisms for Hg^0 removal at low and high temperature were discussed.

GRAPHICAL ABSTRACT

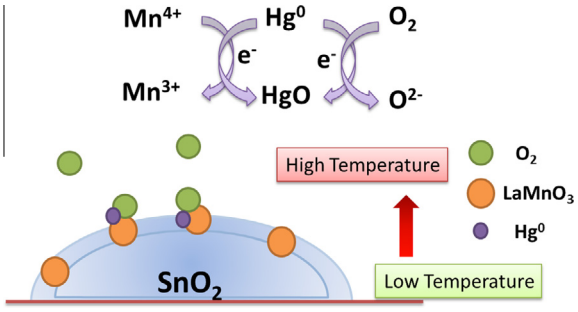

ARTICLE INFO

Article history:
Received 23 November 2015
Received in revised form 18 January 2016
Accepted 19 January 2016
Available online 4 February 2016

Keywords:
Elemental mercury (Hg^0)
Perovskite
SnO_2
Manganese oxide

ABSTRACT

$LaMnO_3/SnO_2$ composite was synthesized as a novel material for the catalytic oxidation and adsorption of elemental mercury (Hg^0). The results indicated that the catalyst having a $LaMnO_3$:SnO_2 = 1:1 M ratio exhibited the highest activity with higher than 99% Hg^0 removal efficiency. $LaMnO_3$ was the primary active sites for Hg^0 catalytic oxidation and adsorption. SnO_2 as catalyst support for $LaMnO_3$ can enlarge the reaction temperature window. The mechanism for Hg^0 removal was discussed by means of XRD, Raman, BET, TEM, H_2-TPR and XPS analysis. The larger surface areas, the more oxygen vacancies and the higher oxidation performance were obtained when SnO_2 acted as catalyst support for $LaMnO_3$. At low temperature, Mn was the primary active sites for Hg^0 catalytic oxidation along with the adsorption by adsorbed-oxygen. With the temperature rising, SnO_2 can adsorb O_2 to form O^{2-} on its surface which was beneficial for the oxidized mercury adsorption. Moreover, SnO_2 exhibited high activity for Hg^0 oxidation when the temperature was higher than 250 °C. The Hg-TPD results indicated that the mercury existed stronger binding state on the surface of $LaMnO_3/SnO_2$.

1. Introduction

Mercury emitted from coal-fired power plants is considered as hazardous atmospheric pollutant [1,2]. Elemental mercury (Hg^0) is the main component of mercury in gaseous phase, and it is difficult to be removed due to its high volatility and low solubility [3]. Adsorption technology is an effective method for the elimination of Hg^0 emission [3–5]. The sorbents for Hg^0 capture are noble metals, transition metal oxides and carbon-based materials [6,7]. Among them, transition metal oxides were widely studied for Hg^0 removal due to the heterogeneous catalytic oxidation of Hg^0 to Hg^{2+} on their surface, following by chemical adsorption with surface oxygen [4,6].

In terms of economical and Hg^0 removal efficiency, Mn-based oxides were regarded as efficient Hg^0 sorbents [7–9]. And they

* Corresponding author. Tel./fax: +86 21 54745591.
E-mail address: nqyan@sjtu.edu.cn (N. Yan).

http://dx.doi.org/10.1016/j.cej.2016.01.078
1385-8947/

presented high redox potential as well as environmental friendly. In previous studies, lots of Mn-based sorbents were synthesized for Hg^0 removal [8,10]. The mechanism for Hg^0 removal can be summarized to two primary steps: (1) catalytic oxidation of Hg^0 to oxidized mercury (Hg^{2+}) along with the reduction of high valance Mn (Mn^{4+}/Mn^{3+}) to low valance of Mn (Mn^{3+}/Mn^{2+}); (2) adsorption of Hg^{2+} with surface O^{2-} to form Hg–O on the surface of the sorbents. Therefore, the enhancement of catalytic oxidation performance and binding state of mercury are two important factors for Hg^0 removal. Among the Mn-based materials, thermally stable perovskite-type oxides (ABO_3) are known to active for the complete oxidation due to their special structure. They were widely used in catalytic oxidation of NO, CO, VOC etc [11,12]. In our recent studies, $LaMnO_3$ perovskite-type oxides had been indicated to be effective for Hg^0 removal, the excellent catalytic oxidation performance was ascribed to the effects of structure and abundant of adsorbed oxygen [13].

However, Mn-based Hg^0 sorbents lost their activity at high temperature (>200 °C) [7,14]. Similarly, $LaMnO_3$ lost its activity for Hg^0 removal at high temperature. The activity was also lost when it was used as de-NO_x catalyst. Thus, $LaMnO_3$ could only be used for low-temperature (<200 °C) de-NO_x catalysts [15,16]. Xie et al. introduced Sn to manganese oxides (MnO_x) to form Sn–MnO_x binary oxides for Hg^0 removal, the reaction temperature window was enlarged by the addition of SnO_2 [14,17]. SnO_2 is a semiconductor which is sensitive to light illumination and thermal energy. SnO_2 has a numbers of intrinsic defects in its structure due to the low formation energies and the strong mutual attraction between tin sites and oxygen vacancies [18]. SnO_2 was intensively studied as gas sensors and lithium rechargeable batteries [18,19]. It was indicated to have superior electrons transfer and oxygen adsorption performance at high temperature. The surface binding oxygen on the SnO_2 (1 1 0) surface was removable and that the surface oxygen vacancies could be formed at the temperature lower than 227 °C [20,21]. These abilities make it possible use as a catalyst support for $LaMnO_3$. To date, as far as we known there was no attempt for the synthesis of $LaMnO_3/SnO_2$ composite as a catalyst or sorbent.

In this work, SnO_2 was first synthesized as catalyst support using a simple precipitation method. And $LaMnO_3/SnO_2$ sorbents were prepared for the investigation of Hg^0 removal performance. The effects of temperature and the molar ratios of $LaMnO_3$ to SnO_2 were studied. The as-prepared materials were tested by means of physical and chemical characterization to discuss the role of SnO_2 in Hg^0 removal process. Mercury desorption performance over $LaMnO_3/SnO_2$ were investigated to show the regeneration performance.

2. Experimental section

2.1. Materials preparation

SnO_2 was synthesized through the precipitation method. A given amount of $SnCl_4$ was dissolved in deionized water under stirring for 1 h. And the stoichiometric amount of ammonia was then added into the above solution. The precipitate was filtrated and washed with deionized water until no Cl^- was detectable in the water. After that the precipitate was transferred to a muffle furnace and calcined at 500 °C for 5 h. The SnO_2 samples were ground to 200–350 mesh for the support. $LaMnO_3$ was synthesized using sol–gel method. In a typical method, the required amount of La $(NO_3)_3$ and $Mn(NO_3)_3$ was dissolved together in diluted water, followed by addition of citric acid (CA) in the mixed solution. The temperature of the aqueous solution was kept constant at 80 °C. The molar ratio for each component was La/Mn/CA = 1:1:2. After vigorous stirring and evaporation, a transparent gel was formed, which was then dried at 90 °C overnight. The obtained precursor was first calcined at 400 °C for 1 h in air to decompose citric acid totally and was then calcined at 750 °C for 5 h with a heating rate of 10 °C/min. The $LaMnO_3/SnO_2$ composite was synthesized using sol–gel method. The mixed solution $La(NO_3)_3$, $Mn(NO_3)_3$ and CA were dissolved together and added into SnO_2 solution, the preparation method was the same to the synthesis process of $LaMnO_3$. The $LaMnO_3$ and SnO_2 molar ratios were set as: 2:1 (LMO_2/Sn_1), 1:1 ($LaMn_3/SnO_2$) and 1:2 (LMO_1/Sn_2). All the prepared samples were grounded to 40–60 mesh.

2.2. Materials characterization

The X-ray diffraction (XRD) tests were conducted with X-ray diffraction with Cu-Kα radiation (APLX-DUO, BRUKER, Germany). The XRD patterns were recorded in the 2θ range from 10° to 80° with scanning rate of 5°/min. The measurements of BET (Brunauer–Emmett–Teller) surface areas were performed using N_2 sorption measurement (Nova-2200 e) at 77 K. The pore volumes of all samples were calculated based on Barrett–Joyner–Halenda (BJH) method. X-ray photoelectron spectroscopy (XPS) was carried out on a Shimadzu–Kratos system to examine the valance states of elements on the surface of materials, coupled with an ultra DLD spectrometer with Al Kα as the excitation source. C 1s line at 284.6 eV was taken as a reference for the binding energy calibration. The reducibility of the samples was conducted by H_2-TPR experiments, it was performed on Chemisorp TPx 290 instrument, the samples were degased at 200 °C for 3 h under Ar atmosphere before the tests, and the reducing gas was 10% H_2/Ar. Raman scattering spectra were performed on a SENTERRA R200. The 633 nm line of Ar^+ laser was used for the excitation. The morphology and structure of the $LaMnO_3$ oxides were observed via a transmission electron microscopy (TEM), and the images were obtained electron microscope (Tecnai G2 Spirit Biotwin) operating at 120 kV.

2.3. Hg^0 removal performance evaluation

The Hg^0 adsorption activities were evaluated using a fixed-bed reactor, the schematic of Hg^0 adsorption system is shown in Fig. S1. An Hg^0 permeation tube was used to generate Hg^0 vapor carried by pure N_2, which was introduced to the inlet of the gas mixer. Other gases such as O_2 were introduced to the gas mixer at constant flows. The mass flow rate was controlled by mass flow controllers (MFC). A fixed-bed reactor system was used to study the Hg^0 adsorption performance. The reaction temperature was controlled from 100 to 300 °C by temperature controller tubular furnace. In each test, the as-prepared materials were placed into the reaction tube. The cold vapor atomic absorption spectroscopy (CVASS) analyzer was used as the online continuous detector. The concentration of Hg^0 was calculated by Lumex RA 915+. The inlet concentration of Hg^0 was 500 ± 50 μg/m^3. At the beginning of each test, the simulated gas bypassed the reactor and the inlet gas was detected to ensure the stable Hg^0 concentration. Then the simulated gas passed the samples and the Hg^0 concentration was detected by CVASS online. To guarantee the gas hourly space velocity (GHSV) was the same ($4.78 * 10^5$ h^{-1}) for each test, different masses of materials were used for tests.

The Hg^0 removal efficiency and the adsorption capacities of Hg^0 were calculated according to Eqs. (1) and (2):

$$\eta_x = \frac{Hg^0_{in} - Hg^0_{out}}{Hg^0_{in}} \quad (1)$$

$$Q = \frac{1}{m}\int_{t2}^{t1}\left(\frac{Hg_{in}{}^0 - Hg^0_{out}}{Hg^0_{in}}\right) * f * dt \quad (2)$$

$$\eta_{oxi} = \frac{Hg^{T}_{out} - Hg^{0}_{out}}{Hg^{0}_{in}} \quad (3)$$

where η_x is the removal efficiency, η_{oxi} is the oxidized mercury, [10]. Hg^0_{in} is the inlet concentration of Hg^0, Hg^0_{out} is the outlet concentration of Hg^0, $Hg_{out}{}^T$ is the concentration of Hg^0_{out} and the oxidized mercury after $SnCl_2$ soulution, Q is the Hg^0 adsorption capacity, m is the mass of the sorbent in the fixed-bed, f is the flow rate of the influent, and t_0 and t_1 are the initial and final test times of the breakthrough curves.

2.4. Hg-TPD method

Mercury temperature programmed desorption (Hg-TPD) method was built to evaluate the desorption performance of as-prepared materials. Before each test, the sorbents were firstly under adsorption for 20 min at 150 °C with 4% O_2 balanced with N_2 (total flow rate = 500 ml/min). After the furnace cooled down to 100 °C, the materials were regenerated by heating from 100 to 700 °C in a pure N_2 carrier gas. The heating rate was set as 5 °C/min. The mercury signal was recorded by CVASS online system.

3. Results and discussion

3.1. Hg^0 removal performance

3.1.1. Effect of temperature on Hg^0 removal performance

The Hg^0 removal performances of $LaMnO_3$, SnO_2 and $LaMnO_3$/SnO_2 were tested in a fixed-bed adsorption system. Fig. 1(a) shows the Hg^0 removal performance at 150 °C with 4% O_2 over these materials. SnO_2 had nearly no activity, and the Hg^0 removal efficiency gradually lost to approximately only 10%. While $LaMnO_3$ exhibited higher Hg^0 removal performance, the Hg^0 removal efficiency was higher than 95% in the initial 200 min. SnO_2 modified $LaMnO_3$ had the highest Hg^0 removal performance with higher than 90% removal efficiency even after 600 min reaction.

To further investigate the role of SnO_2 catalyst support for the modification of $LaMnO_3$, a series of SnO_2 supported $LaMnO_3$ were prepared with different molar ratios of $LaMnO_3$ to SnO_2. The molar ratios of $LaMnO_3$ to SnO_2 were 2:1 (LMO_2/Sn_1), 1:1 ($LaMnO_3/SnO_2$) and 1:2 (LMO_1/Sn_2). As presented in Fig. 1(b), the performances of these materials were investigated at a wide temperature window (100–300 °C) with 4% O_2. The Hg^0 removal efficiencies were calculated based on the total 600 min removal efficiency. For $LaMnO_3$, the highest Hg^0 removal efficiency was 82.9% at 150 °C. The Hg^0 removal efficiency decreased sharply when the temperature increased from 150 to 300 °C, only 40.1% Hg^0 removal efficiency could get at 300 °C. For SnO_2, the Hg^0 removal efficiency was only 5% at 100 °C. However, with the temperature rising, the Hg^0 removal efficiency gradually increased to 65.3% at 300 °C. It was interesting that SnO_2 modification showed good activity for Hg^0 at high temperature. Among the three SnO_2 supported $LaMnO_3$ materials, $LaMnO_3/SnO_2$ had the highest Hg^0 removal performance, the Hg^0 removal efficiency was higher than 99% at 150 and 200 °C, and it can get approximately 70% removal efficiency at 300 °C. LMO_2/Sn_1 also enhanced the performance, the removal efficiency was higher than 99% below 200 °C. But it lost its activity to some extent from 200 to 300 °C. However, the Hg^0 removal efficiency was also higher than that of pure $LaMnO_3$. It was believed that SnO_2 support played an important role for the enhancement of $LaMnO_3$, even at higher temperatures. To further enhance the molar ratio of SnO_2, the performance of LMO_1/Sn_2 was not better than that of $LaMnO_3/SnO_2$. $LaMnO_3/SnO_2$ exhibited the highest performance for Hg^0 removal.

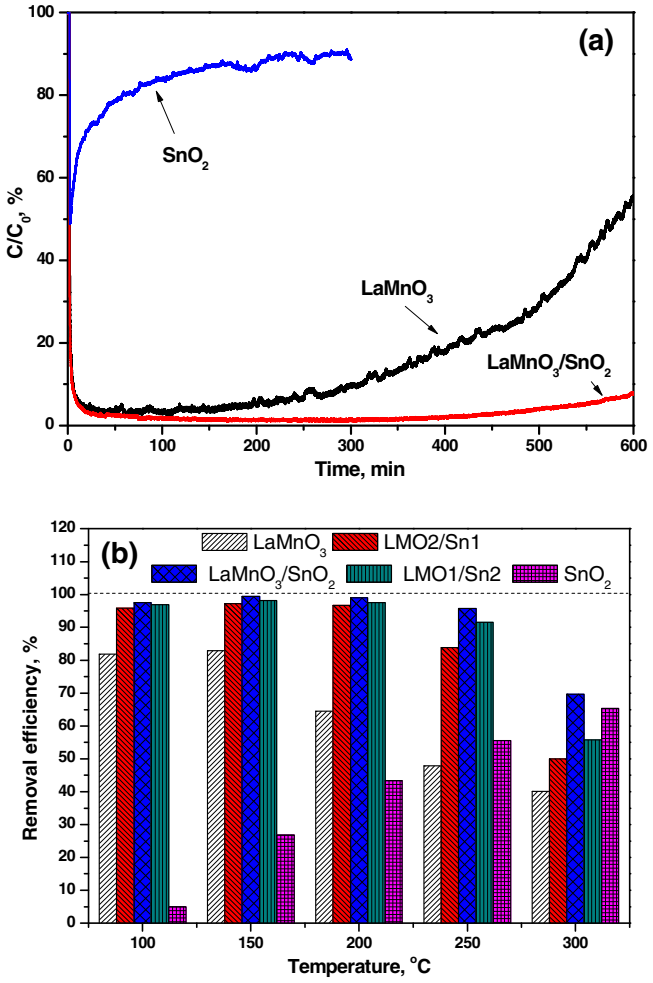

Fig. 1. (a) Hg^0 removal performance over $LaMnO_3$, SnO_2 and $LaMnO_3/SnO_2$; (b) effect of molar ratio of $LaMnO_3$ to SnO_2 on Hg^0 removal efficiency over at 100–300 °C.

3.1.2. Catalytic oxidation and adsorption of Hg^0 over $LaMnO_3/SnO_2$

The results in Fig. 1 indicated that SnO_2 supported $LaMnO_3$ had high activity for Hg^0 removal at high temperature. It could be speculated that SnO_2 had catalytic activity at high temperature for Hg^0, in which O_2 was the oxidant for Hg^0 oxidation. Generally, the concentration of O_2 was ~4% in the real flue gas. To investigate the Hg^0 oxidation and adsorption efficiency over $LaMnO_3/SnO_2$, the effect of O_2 on Hg^0 removal was investigated. As can be seen in Fig. 2, in the absence of O_2 from the simulated gas, the Hg^0 removal efficiency decreased to 80% at 150 °C. The removal efficiencies were further decreased with the temperature rising, and the removal efficiency was only 40% at 300 °C. When the concentration of O_2 was increased to 8% in the simulated gas, the Hg^0 removal efficiency enhanced compared to that of 4% O_2, especially at 300 °C. Obviously, O_2 enhanced the performance of $LaMnO_3/SnO_2$.

A further study was tested to identify the Hg^0 oxidation efficiency and the adsorption state on the surface of $LaMnO_3/SnO_2$. In the absence of O_2, the oxidation efficiency was about 6.5% at 100 °C. When the temperature increased, the oxidation efficiency increased from ~10.5% at 150 °C to 30.2% at 300 °C, respectively. The Hg^0 removal under 4% O_2 indicated that most of Hg^0 was adsorbed on the surface of $LaMnO_3/SnO_2$, lower than 5% Hg^0 oxidation in the outlet of flue gas when the temperature was lower than 150 °C. The Hg^0 oxidation efficiency increased to approximately 10% when the temperature was increased to 200–300 °C. The same phenomenon was found under 8% O_2 atmosphere. The results indi-

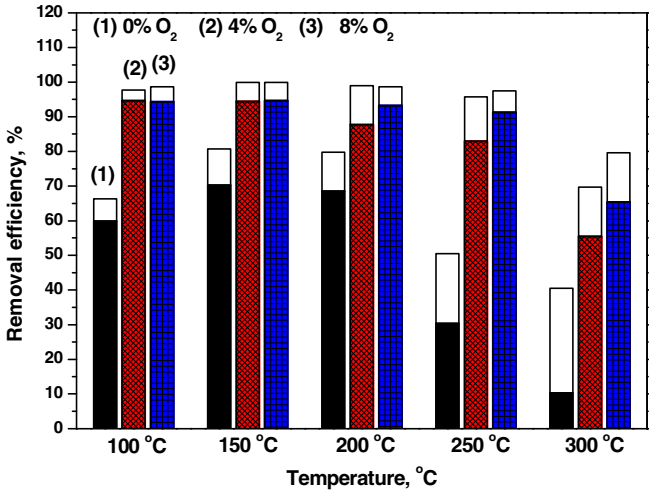

Fig. 2. Hg^0 oxidation and adsorption over $LaMnO_3/SnO_2$ under various O_2 concentrations at the temperature of 100–300 °C.

cated that Hg^0 removal process contained the Hg^0 oxidation in the simulated gas and adsorption on the materials. The deep mechanism was discussed in the following section.

3.1.3. Characterization of SnO_2 supported $LaMnO_3$

The textural properties of as-prepared materials, including the XRD patterns, the BET surface areas, the Raman spectra, and TEM images, were tested and showed in our study. Fig. 3 shows the XRD patterns of the as-prepared samples. For $LaMnO_3$, the peaks at 22.8°, 32.6°, 40.1°, 46.2°, 52.7°, 58.3°, 68.4° and 77.8° were well indexed to the perovskite phase (JPCDS No. 82-1152) with a rhombohedral structure [22]. As shown in Fig. S4, the HRTEM image of $LaMnO_3$ was presented. The lattice can be seen clearly which was perovskite oxide. In addition, the EDX analysis (Fig. S5) further indicated that the compositions were La, Mn and O. $LaMnO_3$ perovskite oxide was successfully synthesized. The SnO_2 samples prepared at 500 °C had tetragonal structure (JPCDS No. 21-1250) [23]. For LMO_2/Sn_1, the added SnO_2 support into the samples, two phases of perovskite and SnO_2 co-existed in the sample. But the phase of SnO_2 was not as obvious as perovskite oxide due to the low concentration of SnO_2. To further enhance the mass of SnO_2 support, the positions of the peaks in $LaMnO_3/SnO_2$ were the same as the LMO_2/Sn_1, but the intensity of SnO_2 was enhanced. Moreover, the half peak width in $LaMnO_3/SnO_2$ pattern became broad, reflecting the smaller particles formed. For LMO_1/Sn_2, the excess SnO_2 didn't change the crystal-form compared with $LaMnO_3/SnO_2$ patterns.

The TEM images show the morphologies of the as-prepared materials (Figs. S2(a–c) and S3(a, b)). As shown in Fig. S2(a), $LaMnO_3$ displayed a bulk morphology with different particle sizes. However, the particles' size of SnO_2 was smaller than that of $LaMnO_3$ (Fig. S2(b)), it was about 11–17 nm. The image of $LaMnO_3/SnO_2$ is shown in Fig. S3(c), it can be seen that the addition of SnO_2 resulted in the porous structure. The bulk structure of $LaMnO_3$ was destroyed which was beneficial for physical-adsorption. The BET surface areas results (Table S1) indicated that $LaMnO_3$, SnO_2 and $LaMnO_3/SnO_2$ had the surface areas of 16.60, 29.89 and 21.77 m^2/g, respectively. Additionally, the addition of SnO_2 enlarged the pore volume of $LaMnO_3$, it was 0.201 cm^3/g for $LaMnO_3/SnO_2$ compared with the 0.118 and 0.141 cm^3/g for $LaMnO_3$ and SnO_2, respectively. For comparison, the TEM images (Fig. S3(a–b)) of LMO_1/Sn_2 and LMO_2/Sn_1 and their surface areas (Table S1) were also tested. The surface areas of LMO_1/Sn_2 and LMO_2/Sn_1 were 18.53 and 20.93 m^2/g, respectively. Among the three SnO_2-modified materials, $LaMnO_3/SnO_2$ showed the highest surface area. Moreover, the morphologies of after SnO_2-modified materials were in porous structure, resulting in the high pore volume. The pore volumes of LMO_1/Sn_2 and LMO_2/Sn_1 were 0.147 and 0.165 cm^3/g, respectively.

To further reveal the structure of SnO_2 catalyst support for $LaMnO_3$, Raman spectroscopy technique was employed and the results are presented in Fig. 4. For comparison, Raman spectra were collected over $LaMnO_3$, LMO_2/Sn_1, $LaMnO_3/SnO_2$, LMO_1/Sn_2 and SnO_2 materials. For SnO_2, three obvious peaks at 473, 630.5 and 695.5 cm^{-1} were detected, they were ascribed to Eg, A_{1g}, B_{1g} vibration [24]. For $LaMnO_3$, the room temperature Raman spectrum of a rhombohedral sample was with broad peaks at 200–700 cm^{-1} [25]. There were no obvious peaks presented in the same intensity to SnO_2. With the addition of SnO_2 to $LaMnO_3$, the Raman shift of SnO_2's peaks became weak which was strongly related to the dispersant effect of $LaMnO_3$ and SnO_2 each other, especially in LMO_2/Sn_1 and LMO_1/Sn_2 spectra [24]. However, when the molar ratio of SnO_2 to $LaMnO_3$ was 1:1, a wide peak at about 500–750 cm^{-1} can be detected, in which could be attributed to the oxygen vacancies in the materials [26]. The abundant oxygen

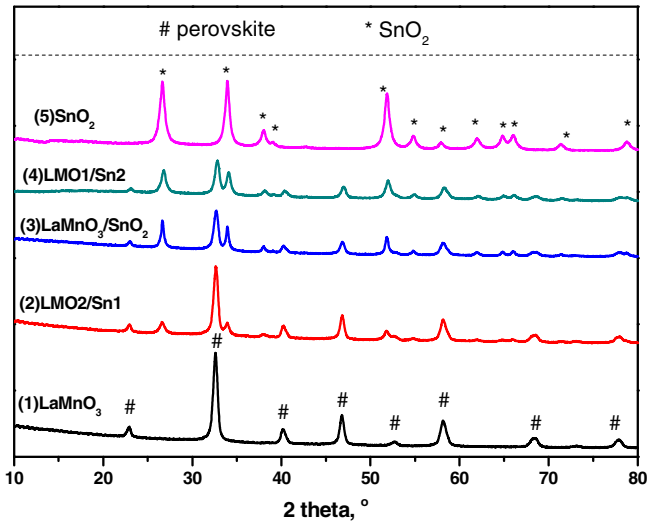

Fig. 3. XRD patterns of the as-prepared samples.

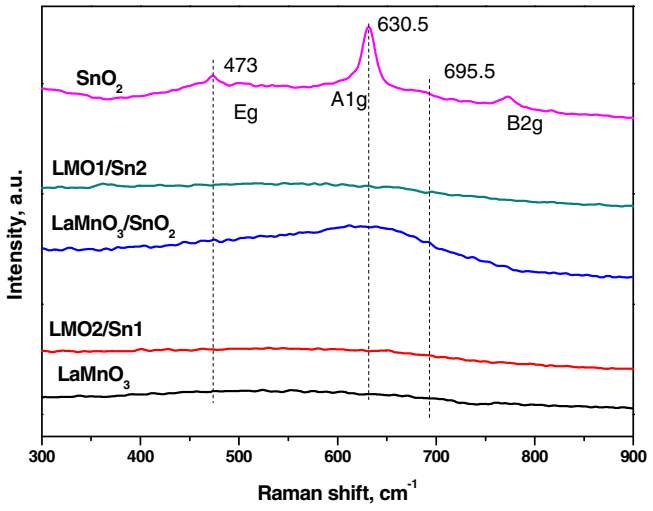

Fig. 4. Raman spectra of $LaMnO_3$, LMO_2/Sn_1, $LaMnO_3/SnO_2$, LMO_1/Sn_2, and SnO_2 materials.

vacancies in the materials were beneficial for higher activity. The results can be well indicated that when the molar ratio of SnO_2 to $LaMnO_3$ was 1:1, $LaMnO_3/SnO_2$ showed the highest activity for Hg^0 removal.

Based on the above discussion, with the addition of SnO_2 as support for $LaMnO_3$, the particle size became small, resulting in the larger surface areas and porous structure. It was favorable for Hg^0 catalytic oxidation and adsorption. Furthermore, the more oxygen vacancies were beneficial for oxygen adsorption which can be used as oxidant for Hg^0 adsorption.

3.2. In-depth study for the mechanism of Hg^0 removal over $LaMnO_3/SnO_2$

3.2.1. $LaMnO_3$ active sits for Hg^0 adsorption at low temperature

As presented above, the larger surface areas, the porous structure and the higher oxygen vacancies were favorable for Hg^0 removal. Based on previous studies, the Mn-based materials for Hg^0 removal highly depended on heterogeneous oxidation and chemical adsorption [10]. The oxidizability and the chemical-adsorption performance were discussed in this section. Fig. 5 displays of the H_2-TPR profiles of as-prepared materials. The H_2-TPR profile of $LaMnO_3$ shows two reduction peaks at 320.1 and 713.0 °C, they were ascribed to the reduction of $Mn^{4+} \rightarrow Mn^{3+}$ and $Mn^{3+} \rightarrow Mn^{2+}$, respectively [22,27]. For pure SnO_2, a shoulder peak can be clearly detected, the peak ranging from about 400 to 900 °C and centered at 698.8 °C, which was attributed to the reduction of SnO_2, as well as $Sn^{2+} \rightarrow$ to Sn^0 [24]. After reduction, tin grains can be obviously found. In the H_2-TPR profile of $LaMnO_3/SnO_2$, a small peak at 325.2 °C, and three peaks at 547.5, 632.3 and 799.5 °C. The reduction peak of $Mn^{4+} \rightarrow Mn^{3+}$ kept at the same temperature (325.2 °C). But the $Mn^{3+} \rightarrow Mn^{2+}$ shifted to the lower temperature. It was speculated that SnO_2 was beneficial for the redox of $Sn^{2+} + Mn^{3+} \leftrightarrow Sn^{4+} + Mn^{2+}$, resulting in the low reduction peaks at 632.3 °C [24]. After Sn^{2+} offered electrons, the Sn^{4+} was re-reduced and the peak was at 547.5 °C. And the reduction peak of $Sn^{2+} \rightarrow Sn^0$ was at 799.5 °C. Therefore, the reducibility of $LaMnO_3$ was improved by SnO_2 support. For comparison, the profiles of LMO_2/Sn_1 and LMO_1/Sn_2 were also illustrated. They showed the same peaks to $LaMnO_3/SnO_2$. The results further indicated SnO_2 acted as a good electrons acceptor during Mn reduction process. The reducibility of $LaMnO_3$ was enhanced by SnO_2 and it was beneficial for Hg^0 oxidation during Hg^0 catalytic oxidation process.

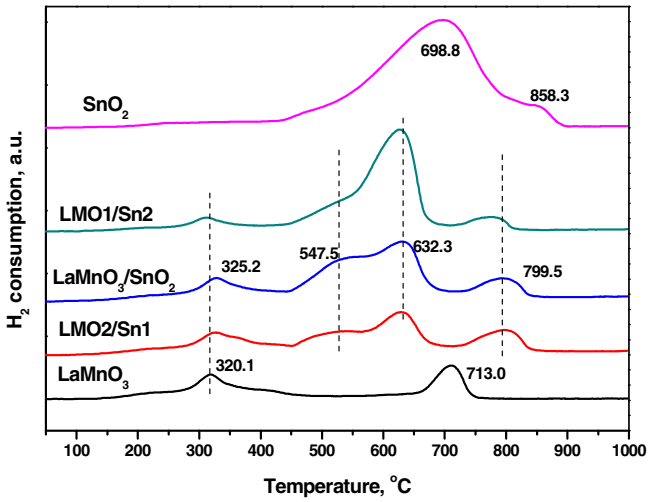

Fig. 5. H_2-TPR profiles of as-prepared materials.

Fig. 6(a) shows O 1s XPS spectra of $LaMnO_3$, LMO_2/Sn_1, $LaMnO_3/SnO_2$, LMO_1/Sn_2 and SnO_2 oxides. For $LaMnO_3$, the bonds at 529.6 and 531.0 eV were ascribed to lattice oxygen (O_{latt}) and adsorbed oxygen (O_{ads}), respectively [10,28]. For LMO_1/Sn_2, LMO_2/Sn_1 and $LaMnO_3/SnO_2$, there were no obvious changes in the positions of these composites. These could be the reason that in the synthesis method, the SnO_2 nanoparticles were firstly synthesized in our study. However, for the O 1s spectra of SnO_2, the peak was centered at 530.9 eV. The higher binding energy was ascribed to the high electron capacity of Sn, resulting in the higher activity of O [10,26,29]. SnO_2 can act as good electron transfer. Fig. 6(b) shows the Mn 2p spectra of as-prepared samples. The peaks at 644.4 and 641.9 eV can be ascribed to Mn^{4+} and Mn^{3+}, respectively [9,10]. There was no peak that can be attributed to Mn^{2+} in the Mn 2p spectra. The ratios of $Mn^{4+}/(Mn^{4+} + Mn^{3+})$ changed in a small range, where $LaMnO_3$ and $LaMnO_3/SnO_2$ had the ratios of 33.93 and 27.21, respectively.

After adsorption, O 1s, Mn 2p and Hg 4f XPS spectra of $LaMnO_3/SnO_2$ are shown in Fig. S6. For O 1s, two peaks can be well defined as O_{ads} and O_{latt}. The ratio of $O_{ads}/(O_{ads} + O_{latt})$ changed from 52.19 to 50.22. And the ratio of $Mn^{4+}/(Mn^{4+} + Mn^{3+})$ changed from 27.21 to 26.32. Interestingly, there was no peaks can be assigned to Mn^{2+} even after adsorption. Based on previous studies, high valance of Mn^{4+} was partly changed to Mn^{3+} of Mn^{2+} after Hg^0 adsorption

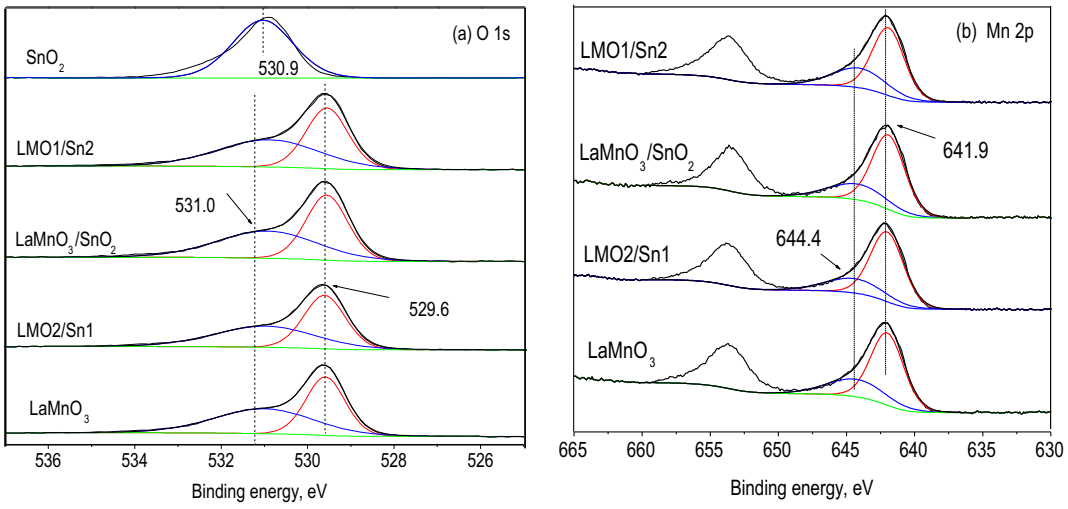

Fig. 6. (a) O 1s and (b) Mn 2p XPS spectra of as-prepared materials.

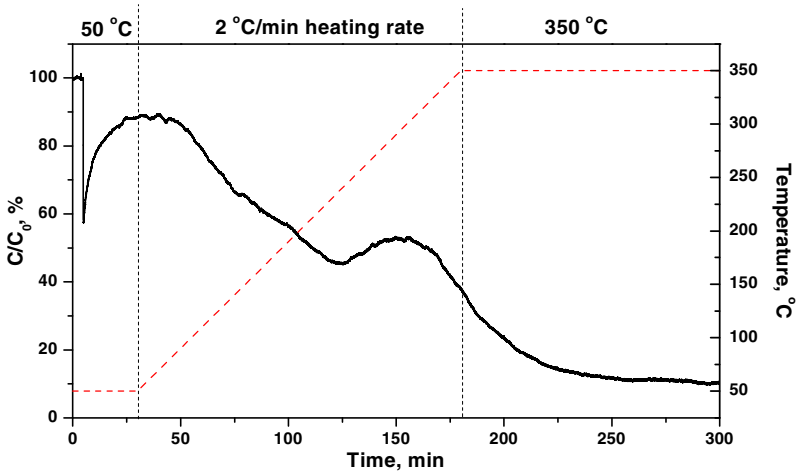

Fig. 7. Hg^0 oxidation over SnO_2 at the heating rate of 2 °C/min.

under the same experimental condition. It was speculated that the reduced Mn (Mn^{2+} or Mn^{3+}) was re-oxidized by O_2, and the SnO_2 can be easily capture the O_2 to refresh the reduced Mn. The Hg 4f spectrum was also observed, two peaks at 102.4 and 105.6 eV for Hg 4f can be ascribed to Hg–O on the surface of $LaMnO_3$/SnO_2. Based on above discussion, the mechanism for Hg^0 capture can be illustrated as follows: [30]

$$Hg^0\ (g) \rightarrow Hg^0\ (ads) \quad (4)$$

$$2Mn^{4+} + Hg^0\ (ads) \rightarrow 2Mn^{3+} + Hg^{2+}\ (ads) \quad (5)$$

$$Hg^{2+}\ (ads) + O^{2-}\ (ads) \rightarrow Hg^0\ (ads) \quad (6)$$

3.2.2. Enhancement of heterogeneous catalytic oxidation of Hg^0

Based on the above results, SnO_2 catalyst support enhanced $LaMnO_3$'s Hg^0 removal performance, especially at high temperature. The catalytic oxidation experiments further indicated that with the addition of SnO_2, the Hg^0 can be oxidized to oxidation state at high temperature. Herein, the experiment was designed to investigate the oxidation capacity over SnO_2. As can be seen from Fig. 7, when the temperature was 50 °C, SnO_2 had little activity for Hg^0. After the temperature programmed rising (10 °C/min), the Hg^0 removal efficiency gradually increased. The peak at ~300 °C could be the result of Hg^0 desorption from the surface of SnO_2. When the temperature reached to 350 °C, the Hg^0 removal efficiency was as high as 90%. Obviously, SnO_2 had high catalytic oxidation performance for Hg^0. In previous studies, SnO_2 was confirmed to have excellent O_2 adsorption performance, O_2 in the gas can be firstly adsorbed on the surface to get physical-adsorbed O_2 (O_2(p-ads)). With the temperature rising, the O_2(p-ads) changed to chemical-adsorbed O_2 (O_2(p-ads)) along with the electron transfer. The XPS results indicated that SnO_2 had active O_2 on its surface. The mechanism can be written as follows: [20]

$$O_2\ (g) \rightarrow O_2\ (p\text{-}ads) \quad (7)$$

$$O_2\ (p\text{-}ads)e^- \rightarrow O_2^-\ (c\text{-}ads) \quad (8)$$

$$O_2^-\ (c\text{-}ads)e^- \rightarrow 2O^-\ (c\text{-}ads) \quad (9)$$

$$O^-(c\text{-}ads) + e^- \rightarrow O^{2-}(c\text{-}ads) \quad (10)$$

When SnO_2 acted as support for $LaMnO_3$, the abundant oxygen vacancies on its surface offered the opportunity for O_2 capture which was beneficial for Hg^0 adsorption. The high catalytic oxidation performance of SnO_2 significant enhanced the heterogeneous catalytic oxidation of $LaMnO_3$.

3.2.3. Enhancement of adsorption at high temperature

The Hg^0 removal mechanism was primary attributed to a chemical adsorption process over Mn-based oxides. The Hg-TPD method was built to test the binding state of mercury of the materials. As can be seen in Fig. 8, a strong peak at 361.5 °C for $LMnO_3$. For $LaMnO_3$/SnO_2, a strong peak at 372.0 °C and a weak peak at 467.5 °C, respectively. For SnO_2, two weak peaks at 263.5 and 502.5 °C can be indexed to the physical-adsorption and chemical-adsorption of mercury on its surface. Therefore, SnO_2 enlarged the Hg^0 adsorption capacity of $LaMnO_3$ because the strong binding bond between oxidized mercury and $LaMnO_3$/SnO_2. The Hg-TPD results also give us a method for the sorbents regeneration, mercury adsorbed on the surface of $LaMnO_3$/SnO_2 could be released by simple thermal desorption method.

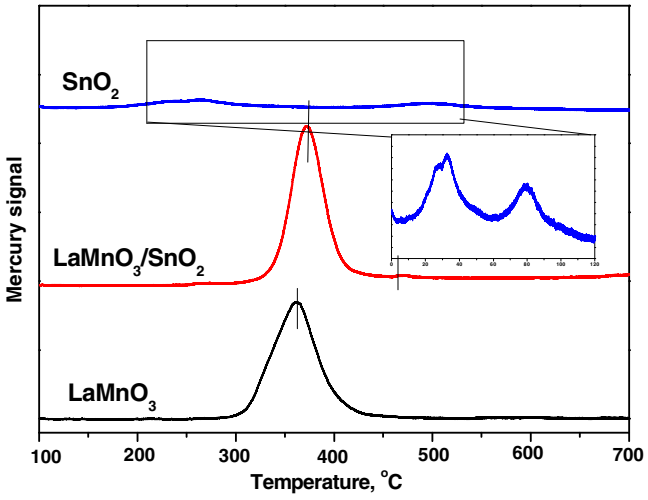

Fig. 8. Hg-Tpd curves of $LaMnO_3$, $LaMnO_3$/SnO_2 and SnO_2 at the heating rate of 5 °C/min.

Herein, with the addition of SnO_2 as supports for $LaMnO_3$, $LaMnO_3/SnO_2$ showed higher Hg^0 removal performance, especially at high temperature. The excellent catalytic oxidation performance of SnO_2 at higher temperature enlarged the Hg^0 removal performance. SnO_2 can be used as a catalyst support for the modification of $LaMnO_3$ due to its structure-effect, high catalytic oxidation and electrons transfer performances. These properties can be made full use as catalytic decomposition of other pollutants in subsequent research work.

The sketch of flow process for Hg^0 removal, the TEM images of TEM images of (1) LMO_2/Sn_1 and (2) LMO_1/Sn_2, the O 1s, Mn 2p and Hg 4f XPS spectra of $LaMnO_3/SnO_2$ after adsorption, the BET and XPS results are illustrated in supporting information.

Acknowledgements

This study was supported by the Major State Basic Research Development Program of China (973 Program, No. 2013CB430005), and the National Natural Science Foundation of China (No. 51478261 and No. 51278294). Thanks for Shanghai Tongji Gao Tingyao Environmental Science and Technology Development Foundation.

Appendix A. Supplementary data

Supplementary data associated with this article can be found, in the online version, at http://dx.doi.org/10.1016/j.cej.2016.01.078.

References

[1] C.L. Senior, A.F. Sarofim, T. Zeng, J.J. Helble, R. Mamani-Paco, Gas-phase transformations of mercury in coal-fired power plants, Fuel Process. Technol. 63 (2000) 197–213.
[2] M. Gustin, H. Amos, J. Huang, M. Miller, K. Heidecorn, Measuring and modeling mercury in the atmosphere: a critical review, Atmos. Chem. Phys. 15 (2015) 5697–5713.
[3] J.H. Pavlish, E.A. Sondreal, M.D. Mann, E.S. Olson, K.C. Galbreath, D.L. Laudal, S. A. Benson, Status review of mercury control options for coal-fired power plants, Fuel Process. Technol. 82 (2003) 89–165.
[4] H. Yang, Z. Xu, M. Fan, A.E. Bland, R.R. Judkins, Adsorbents for capturing mercury in coal-fired boiler flue gas, J. Hazard. Mater. 146 (2007) 1–11.
[5] Y. Gao, Z. Zhang, J. Wu, L. Duan, A. Umar, L. Sun, Z. Guo, Q. Wang, A critical review on the heterogeneous catalytic oxidation of elemental mercury in flue gases, Environ. Sci. Technol. 47 (2013) 10813–10823.
[6] A.A. Presto, E.J. Granite, Survey of catalysts for oxidation of mercury in flue gas, Environ. Sci. Technol. 40 (2006) 5601–5609.
[7] S. Qiao, J. Chen, J. Li, Z. Qu, P. Liu, N. Yan, J. Jia, Adsorption and catalytic oxidation of gaseous elemental mercury in flue gas over MnO_x/alumina, Ind. Eng. Chem. Res. 48 (2009) 3317–3322.
[8] J. Li, N. Yan, Z. Qu, S. Qiao, S. Yang, Y. Guo, P. Liu, J. Jia, Catalytic oxidation of elemental mercury over the modified catalyst Mn/α-Al_2O_3 at lower temperatures, Environ. Sci. Technol. 44 (2009) 426–431.
[9] H. Li, C.-Y. Wu, Y. Li, J. Zhang, Superior activity of MnO_x–CeO_2/TiO_2 catalyst for catalytic oxidation of elemental mercury at low flue gas temperatures, Appl. Catal. B 111 (2012) 381–388.
[10] C. He, B. Shen, J. Chen, J. Cai, Adsorption and oxidation of elemental mercury over Ce-MnO_x/Ti-PILCs, Environ. Sci. Technol. 48 (2014) 7891–7898.
[11] N. Russo, D. Fino, G. Saracco, V. Specchia, Studies on the redox properties of chromite perovskite catalysts for soot combustion, J. Catal. 229 (2005) 459–469.
[12] J. Zhu, H. Li, L. Zhong, P. Xiao, X. Xu, X. Yang, Z. Zhao, J. Li, Perovskite oxides: preparation characterizations, and applications in heterogeneous catalysis, ACS Catal. 4 (2014) 2917–2940.
[13] H. Xu, Z. Qu, C. Zong, F. Quan, J. Mei, N. Yan, Catalytic oxidation and adsorption of Hg^0 over low-temperature NH_3-SCR $LaMnO_3$ perovskite oxide from flue gas, Appl. Catal. B: Environ. (2015).
[14] J. Xie, H. Xu, Z. Qu, W. Huang, W. Chen, Y. Ma, S. Zhao, P. Liu, N. Yan, Sn–Mn binary metal oxides as non-carbon sorbent for mercury removal in a wide-temperature window, J. Colloid Interface Sci. 428 (2014) 121–127.
[15] R. Zhang, W. Yang, N. Luo, P. Li, Z. Lei, B. Chen, Low-temperature NH_3-SCR of NO by lanthanum manganite perovskites: effect of A-/B-site substitution and TiO_2/CeO_2 support, Appl. Catal. B 146 (2014) 94–104.
[16] R. Zhang, N. Luo, W. Yang, N. Liu, B. Chen, Low-temperature selective catalytic reduction of NO with NH_3 using perovskite-type oxides as the novel catalysts, J. Mol. Catal. A: Chem. 371 (2013) 86–93.
[17] H. Xu, J. Xie, Y. Ma, Z. Qu, S. Zhao, W. Chen, W. Huang, N. Yan, The cooperation of FeSn in a MnO_x complex sorbent used for capturing elemental mercury, Fuel 140 (2015) 803–809.
[18] A. Kolmakov, D. Klenov, Y. Lilach, S. Stemmer, M. Moskovits, Enhanced gas sensing by individual SnO_2 nanowires and nanobelts functionalized with Pd catalyst particles, Nano Lett. 5 (2005) 667–673.
[19] X.W. Lou, Y. Wang, C. Yuan, J.Y. Lee, L.A. Archer, Template-free synthesis of SnO_2 hollow nanostructures with high lithium storage capacity, Adv. Mater. 18 (2006) 2325–2329.
[20] S. Park, S. An, Y. Mun, C. Lee, UV-enhanced NO_2 gas sensing properties of SnO_2-core/ZnO-shell nanowires at room temperature, ACS Appl. Mater. Interfaces 5 (2013) 4285–4292.
[21] J. Yan, E. Khoo, A. Sumboja, P.S. Lee, Facile coating of manganese oxide on tin oxide nanowires with high-performance capacitive behavior, ACS Nano 4 (2010) 4247–4255.
[22] Y. Liu, H. Dai, Y. Du, J. Deng, L. Zhang, Z. Zhao, C.T. Au, Controlled preparation and high catalytic performance of three-dimensionally ordered macroporous $LaMnO_3$ with nanovoid skeletons for the combustion of toluene, J. Catal. 287 (2012) 149–160.
[23] T. Xingfu, L. Junhua, W. Lisi, H. Jiming, MnO_x–SnO_2 catalysts synthesized by a redox coprecipitation method for selective catalytic reduction of NO by NH_3, Chin. J. Catal. 29 (2008) 531–536.
[24] C. Liu, H. Xian, Z. Jiang, L. Wang, J. Zhang, L. Zheng, Y. Tan, X. Li, Insight into the improvement effect of the Ce doping into the SnO_2 catalyst for the catalytic combustion of methane, Appl. Catal. B 176 (2015) 542–552.
[25] N. Dodiya, D. Varshney, Structural properties and Raman spectroscopy of rhombohedral $La_{1-x}Na_xMnO_3$ $0.075 \leqslant x \leqslant 0.15$, J. Mol. Struct. 1031 (2013) 104–109.
[26] H. Chang, X. Chen, J. Li, L. Ma, C. Wang, C. Liu, J.W. Schwank, J. Hao, Improvement of activity and SO_2 tolerance of Sn-modified MnO_x–CeO_2 catalysts for NH3-SCR at low temperatures, Environ. Sci. Technol. 47 (2013) 5294–5301.
[27] C. Zhang, C. Wang, W. Zhan, Y. Guo, Y. Guo, G. Lu, A. Baylet, A. Giroir-Fendler, Catalytic oxidation of vinyl chloride emission over $LaMnO_3$ and $LaB_{0.2}Mn_{0.8}O_3$ (B = Co, Ni, Fe) catalysts, Appl. Catal. B 129 (2013) 509–516.
[28] S. Yang, Y. Guo, N. Yan, Z. Qu, J. Xie, C. Yang, J. Jia, Capture of gaseous elemental mercury from flue gas using a magnetic and sulfur poisoning resistant sorbent Mn/γ-Fe_2O_3 at lower temperatures, J. Hazard. Mater. 186 (2011) 508–515.
[29] X. Yao, Y. Xiong, W. Zou, L. Zhang, S. Wu, X. Dong, F. Gao, Y. Deng, C. Tang, Z. Chen, Correlation between the physicochemical properties and catalytic performances of $Ce_xSn_{1-x}O_2$ mixed oxides for NO reduction by CO, Appl. Catal. B 144 (2014) 152–165.
[30] H. Xu, Z. Qu, C. Zong, W. Huang, F. Quan, N. Yan, MnOx/graphene for the catalytic oxidation and adsorption of elemental mercury, Environ. Sci. Technol. (2015).